OBS noise reduction from horizontal and vertical components using harmonic-percussive separation algorithms

Zahra Zali[1,2], Theresa Rein[1], Frank Krüger[1], Matthias Ohrnberger[1], Frank Scherbaum[1]

[1]University of Potsdam, Institute of Geosciences, Karl-Liebknecht-Str. 24-25, 14476 Potsdam, Germany

[2]GFZ German Research Centre for Geosciences, Potsdam, Germany

Correspondence to: Zahra Zali (zali@uni-potsdam.de)

Zahra Zali: Campus Golm, Building 29, Room 2.48, Karl-Liebknecht-Str. 24-25, 14476 Potsdam, Germany (zali@uni-potsdam.de)

Theresa Rein: Campus Golm, Building 27, Room 0.43, Karl-Liebknecht-Str. 24-25, 14476 Potsdam, Germany (theresa.rein@uni-potsdam.de)

Frank Krüger: Campus Golm, Building 27, Room 1.36, Karl-Liebknecht-Str. 24-25, 14476 Potsdam, Germany (Frank.Krueger@geo.uni-potsdam.de)

Matthias Ohrnberger: Campus Golm, Building 27, Room 1.37, Karl-Liebknecht-Str. 24-25, 14476 Potsdam, Germany (Matthias.Ohrnberger@geo.uni-potsdam.de)

Frank Scherbaum: Campus Golm, Building 29, Room 1.52, Karl-Liebknecht-Str. 24-25, 14476 Potsdam, Germany (Frank.Scherbaum@geo.uni-potsdam.de)

Abstract

Records from ocean bottom seismometers (OBS) are highly contaminated by noise, which is much stronger compared to data from most land stations, especially on the horizontal components. As a consequence, the high energy of the oceanic noise at frequencies below 1 Hz considerably complicates the analysis of the teleseismic earthquake signals recorded by OBSs.

Previous studies suggested different approaches to remove low-frequency noises from OBS recordings, but mainly focused on the vertical component. The records of horizontal components, crucial for the application of many methods in passive seismological analysis of body and surface waves, could not be much improved in the teleseismic frequency band. Here we introduce a noise reduction method, which is derived from the harmonic-percussive separation algorithms used in Zali et al., (2021) in order to separate long-lasting narrowband signals from broadband transients in the OBS signal. This leads to significant noise reduction of OBS records on both the vertical and horizontal components and increases the earthquake signal-to-noise ratio (SNR) without distortion of the broadband earthquake waveforms. This is demonstrated through tests with synthetic data. Both SNR and cross-correlation coefficients showed significant improvements for different realistic noise realizations. The application of denoised signals in surface wave analysis and receiver functions is discussed through tests with synthetic and real data.

1 Introduction

Ocean bottom seismometer recordings are generally difficult to analyze, because the noise level is usually much higher compared to land stations. At frequencies below 1 Hz, the effect of the ocean noise is often dominating the data and hinders the seismological analysis (e.g. Webb et al., 1991; Crawford, 1994). Signals of interest, i.e. transient signals, especially from teleseismic events can be masked by the oceanic noise. Here, the horizontal components are most strongly contaminated by low frequency noise. To illustrate the noise on OBS data, we exemplary show the records of the station D10 of the DOCTAR array (see Fig. 1 and Fig. S1). Various studies tried to identify and characterize the different sources of noise recorded at the ocean bottom (e.g. Webb, 1998; Crawford & Webb, 2000; Corela, 2014; Stähler et al., 2018; Essing et al., 2021; An et al., 2021). In our study, we focus on noise sources that especially affect teleseismic horizontal recordings in the frequency band of 0.02–2 Hz. Generally, the dominant natural noise signals in the oceanic environment are secondary oceanic microseisms (Rayleigh/Scholte waves at the ocean bottom) caused by the interaction of wind-generated water waves, infragravity waves (compliance noise) as well as tilt noise; the latter is originating from the turbulent interaction between currents and the instrument (e.g. Crawford et al., 1998; Corela, 2014). Primary oceanic microseism is originating from the interaction of water waves incident at steep coastlines and/or rough seafloor (Hasselmann, 1963; Webb, 1998; Bell et al., 2015). Its spectral peak is around 0.07 Hz (Friedrich et al. 1998) in the Northern Atlantic. The secondary microseism has frequencies above 0.1–0.25 Hz, with a highest spectral peak around 0.14 Hz (Friedrich et al., 1998, Fig. 1). It is caused by wind or swell waves propagating in opposite directions. The primary and secondary microseisms affect both the vertical and

Zahra Zali 28.11.2022 13:48
Deleted: higher

Zahra Zali 28.11.2022 13:49
Deleted: the data… but mainly focus… [1]

Zahra Zali 28.11.2022 13:53
Deleted: Data from …o…ean bottom… [2]

horizontal seismometer components, whereas the compliance noise is solely observed on the vertical component and the hydrophone. Compliance noise, dominant in the frequency band of 0.01–0.04 Hz, is only significant if its wavelength exceeds the water depth (Crawford et al., 1998; Crawford & Webb, 2000; Bell et al., 2015).

Below frequencies of 0.01 Hz and 0.1 Hz, the vertical and especially the horizontal components, are highly contaminated by tilt noise generated by ocean bottom currents (Webb, 1998; Crawford& Webb, 2000; Stähler et al., 2018, Fig. 1). The tilt noise level increases with signal period (see Fig. 1). The ocean bottom currents in many regions of the oceans are mostly driven by tidal force and often create a signal with strongest amplitudes below 1 Hz, appearing every 6–12 hours (e.g. Brink, 1995; Crawford & Webb, 2000; Ramakrushana Reddy et al., 2020; Essing et al., 2021). The ocean bottom currents passing the instrument create local eddy currents, deform the seafloor beneath the sensor and tilt the whole instrument frame, to which the seismometer is fixed (e.g. Duennebier & Sutton, 1995; Webb, 1998; Romanowicz et al., 1998; Crawford & Webb, 2000; Corela, 2014; Stähler et al., 2018). If the seismometer mass is not perfectly leveled, the high tilt noise on the horizontal components is partially projected onto the vertical component (e.g. Crawford, 1994; Corela, 2014; Bell et al., 2015). Since the noise sources often act at frequencies of teleseismic earthquakes, it is crucial to improve the signal-to-noise ratio (SNR) on OBS recordings for the analysis of the Earth's crustal and mantle structure. Various studies discussed the improvement of OBS recordings through different approaches, either by suggesting a better OBS instrument design (Stähler et al., 2018, Corela, 2014, Essing et al., 2021), or by removing significant amounts of the noise from the contaminated data by signal processing (Crawford & Webb, 2000, Bell et al., 2015, Janiszewski et al., 2019). Our study follows the latter approach.

Crawford and Webb (2000) developed a method to remove noise from the vertical OBS component. Calculating the linear transfer function between the horizontal and the vertical component allows estimating the tilt noise which then can be subtracted from the vertical component. Hydrophone data measured in parallel to the seismometer recordings allow reducing the influence of infragravity waves on the vertical seismometer component recordings. For better results, Bell et al. (2015) propose to first rotate the horizontal components into the direction of the highest coherence between the horizontal and vertical component before calculating the linear transfer functions. The mentioned methods solely improve the SNR on the vertical component whereas the noise contamination on horizontal components is often larger. Other recent studies attempted to reduce noise also on the horizontal components (Mousavi and Langston, 2017; Zhu et al., 2019; An et al., 2021; Negi et al., 2021). An et al. (2021) tried to reduce the noise on the horizontal components by applying the reversed procedure of Bell et al. (2015). Rotation of one horizontal component into the direction of the principle noise indeed results in an improvement of the orthogonal horizontal component, but the other horizontal component became noisier (An et al., 2021). Results of a recent study applying a polarization filter to reduce the noise on all components show strong changes of the broadband waveforms (Negi et al., 2021). The automatic noise-attenuation method developed by Mousavi and Langston (2017) is a time-frequency denoising algorithm using the wavelet transform and

Zahra Zali 28.11.2022 14:01
Deleted: the

Zahra Zali 28.11.2022 14:02
Deleted: to estimate

Zahra Zali 28.11.2022 14:02
Deleted: to reduce

synchrosqueezing. It can be either used to keep the signal and remove the noise or vice versa. The decomposition method DeepDenoiser from Zhu et al. (2019) is based on a deep neural network. DeepDenoise decomposes the waveform into signal and noise in the time-frequency domain. The latter methods, both improve the SNR, but mainly focus on local and regional earthquake detection. They result in changes in the waveform shape if the noise amplitude directly ahead of the signal is significant in comparison to the signal amplitude in a specific frequency. However, the analysis of undistorted broadband waveforms on the horizontal components is crucial for many passive seismological structure analysis methods, e.g. the calculation of receiver functions or surface wave dispersion and polarization analysis.

Here we introduce a method, inspired from the music information retrieval (MIR) research, which is adapted to seismological data and is used for noise reduction on both, the vertical and the horizontal components.

Seismic waveforms and acoustic signals generated by musical instruments are similar in some aspects (Schlindwein et al., 1995; Johnson and Watson, 2019). The extensive research in the field of music information retrieval has resulted in advances (e.g., Müller, 2015) that may be useful in seismic signal processing as well. Exploiting the idea of harmonic-percussive separation (HPS) in MIR, Zali et al. (2021) developed an algorithm to separate harmonic volcanic tremor from earthquakes in seismic waveforms. In the present study we use this algorithm after some modifications in order to separate 'harmonic' (long-lasting narrowband signals) and 'percussive' (broadband transients) components of an OBS data set aiming at noise reduction and retrieval of clearer broadband earthquake waveforms. Throughout this study we will make use of the term noise for any signal other than earthquake signal in the data set. In the context of OBS noise reduction using HPS algorithms, percussive components correspond to earthquake signals and harmonic components correspond to noise signals. The long-duration OBS noise signals that last a few hours to days (depending on the noise type) with a restricted frequency range contrasts with transient seismic signals such as earthquakes with a wider range of frequencies.

The algorithm introduced in Zali et al., (2021) is a combination of two HPS approaches that leads to the desired signal separation. Here we also use the two approaches subsequently in order to separate different type of noise signals from the earthquake signals. In the first step we adopt HPS using a similarity matrix (Rafii and Pardo, 2012; Rafii et al., 2014) to separate monochromatic and harmonic noises. In the second step we adopt HPS using median filtering (FitzGerald, 2012) in order to separate the remaining narrow-band signals. With this two-step approach we can separate and remove much of the OBS noise contamination from the earthquake signals.

2 Data

In this study we discuss the noise recorded by a LOBSTER (Longterm OBS for Tsunami and Earthquake Research) OBS instrument from the DEPAS pool, which is equipped with a Güralp CMG-40T seismometer, a MCS (Marine compact seismic) recorder and loose cables (for technical specification see Stähler et al., 2018). We show data recorded during the DOCTAR deployment, using DEPAS-LOBSTERs,

Zahra Zali 28.11.2022 14:03
Deleted: and

Zahra Zali 28.11.2022 15:01
Deleted: the DEPAS Pool web page and Alfred-Wegener-Institute, Helmholtz-Zentrum für Polar- und

located around the Gloria Fault in the Northern Atlantic. Twelve DEPAS-LOBSTERs form the array. They were deployed between 2011-2012 and recorded the data with a sampling frequency of 100 Hz (Hannemann et al., 2016; Hannemann et al., 2017).

Until 2019 the DEPAS LOBSTER OBS was built with an OBS-specific version of the Güralp CMG-40T/MCS recorder, where the seismometer had a corner frequency of 60 s and has been modified to last long on the seafloor (Stähler et al., 2018). However, the development of less power consumption lead to a higher noise level of the instrument itself (Stähler et al., 2018). At low frequencies (<0.1 Hz) the self-noise of the sensor is highly affecting the records, especially on the vertical component. However, the design of the DEPAS-LOBSTERs has been improved for deployments after 2019 (e.g. Essing et al., 2021).

We observed a continuous harmonic signal at a frequency of 0.04 Hz, partially with one or two overtones on a subset of the array (see Fig. 1). This signal was observed on 30% of the stations from the DOCTAR project (e.g., Hannemann et al, 2016, Hannemann et al., 2017) and on 43% of the stations from the KNIPAS project (Schlindwein et al., 2018), both using the mentioned DEPAS-LOBSTER design. We cannot identify the source of this signal yet, but based on its continuity, we assume an electronic source from the instrument itself.

The hydrophone and especially the horizontal components are highly affected by the strumming of the head-buoy, which is attached to the DEPAS-LOBSTER frame causing a 'current-induced harmonic tremor signal' (Stähler et al., 2018; Essing et al., 2021, Fig. 1). These 'tremor events' last over up to 4 hours and appear every 6–12 hours. These presumably tidal-driven tremor events are harmonic signals with a fundamental period of 0.4–1 s and various overtones (1–10 Hz) (Stähler et al., 2018; Essing et al., 2021, Fig. 1). Regarding the frequency band, 'tremor events' mainly affect the analysis of teleseismic body waves, especially on the horizontal component (Fig. 1).

Zahra Zali 28.11.2022 14:18
Deleted: 'current

3 Noise reduction methodology

3.1 Harmonic-percussive separation (HPS)

Harmonic-percussive separation refers to the problem of decomposing a signal into its harmonic and percussive components. This topic has received much attention in recent years (Rafii et al., 2018) and has numerous applications in the field of MIR and musical signal processing.

Within a general context harmonic signals show an overtone structure in the spectral domain. We call overtones one or more clear narrow-banded frequency peaks being integer multiples of the fundamental frequency (the first frequency peak in the spectrum). Harmonic signals have a relatively stable behavior

over time and can be identified in a Short Time Fourier Transform (STFT) spectrogram by horizontal structures referred to constant frequencies along the time axis.

In contrast, percussive signals form vertical structures in a STFT spectrogram that contain energy in a wide range of frequencies. Therefore it is a straightforward strategy in most HPS algorithms to try to separate the horizontal structure from the vertical structure in the spectrogram corresponding to harmonic and percussive components, respectively. The horizontal lines in the spectrogram could correspond to either harmonic signals or monochromatic signals.

OBS noise forms narrowband horizontal structures in the STFT spectrogram while earthquake signals have vertical exhibition in the STFT spectrogram.

3.2 HPS using median filtering (MED)

In the context of HPS, one of the simplest and fastest approaches is median filtering (FitzGerald, 2010). For simplification we name this algorithm as MED in this study. Median filters are usually used to remove noise from an image or a signal. Using a median filter a sample will be replaced by the median of neighboring samples within a window of a specific length (The specific length is the kernel size of the median filter). The entire signal is processed using a sliding window analysis. Within the HPS, two median filters are applied to the amplitude of the STFT spectrogram of a signal. One median filter is performed along the time axis of the spectrogram to suppress percussive events and enhance harmonic components. Another median filter is applied along the frequency axis in order to enhance percussive events and suppress harmonic components. The two resulting spectrograms are then subsequently used to create two masks, which are applied to the original signal spectrogram separately to generate two spectrograms of harmonic and percussive components, respectively. For creating the harmonic and percussive signals in the time domain the phase of the original signal is added to each spectrogram and the time domain signals are reconstructed using the inverse STFT.

Zahra Zali 28.11.2022 14:08
Deleted: A

3.3 HPS using the similarity matrix (SIM)

Another powerful approach in HPS proposed by Rafii & Pardo (2012) is based on calculating a similarity matrix. We name this algorithm as SIM here. This approach is a repetition-based separation, which identifies repeating elements in the spectrogram by looking for similarities by means of a similarity matrix. Within the SIM algorithm, first similar time frames in the spectrogram are identified through a similarity matrix. Then a median filter is applied only to the frames identified as similar to constitute the repeating spectrogram model that corresponds to harmonic components. The non-repeating spectrogram that corresponds to the percussive component of the data is obtained by subtracting the repeating spectrogram from the original spectrogram. For creating the repeating and nonrepeating signals in the time domain, the

Zahra Zali 28.11.2022 14:10
Deleted: the

Zahra Zali 28.11.2022 14:09
Deleted: in

phase of the original signal is added to each spectrogram and the time domain signals are reconstructed using the inverse STFT. Details of this approach are discussed in the following section.

3.4 HPS noise reduction algorithm for OBS data

The motivation for using HPS for noise reduction of OBS data stems from the different characteristic of earthquake and OBS noise signals as described in Sect. 2. Earthquakes are broadband transient signals, while the signals of OBS noises are more narrow-band compared to earthquakes. We combine two modified HPS algorithms to separate those signals in a two-step procedure. We divide the frequency content of the signal into two frequency ranges; range one covers the frequency range between 0.1 to 1 Hz whereas range two contains the complementary frequency range, i.e. all frequencies except the band between 0.1 and 1 Hz. Then two different algorithms are applied to range one and range two, respectively. In the first step, we use the SIM algorithm and separate only harmonic or monochromatic signals from the original records in range two avoiding the frequency range of 0.1 to 1 Hz. The reason is related to the frequency content of the noise and earthquake signals and how the SIM algorithm separates them. For a better understanding, we first explain how the algorithm works and then present more detail about this selection. In the second step, to reduce noise from the specified frequency range we apply MED. There we target harmonic (or monochromatic) as well as narrow-band signals with gliding frequencies named as current-induced harmonic tremor signal in the Sect. 2. The overall schematic diagram of our HPS noise reduction algorithm along with an example is shown in Fig. 2.

The SIM algorithm is explained in the following: From the original OBS record SO (SO represents the original restituted OBS signal) we derive the STFT named X being a complex-valued spectrogram.

The complex-valued spectrogram $\mathbf{X}$ is separated into its amplitude and phase components using Eq. 1.

$$X = V * exp(1j * \varphi), \tag{1}$$

where φ is the phase of $\mathbf{X}$, $\mathbf{V} = |\mathbf{X}|$ is the amplitude of $\boldsymbol{X}$ and j is the imaginary unit.

All of the spectrogram modifications will be applied to the amplitude spectrogram $\mathbf{V}$. The cosine similarity (the similarity between two vectors of an inner product space) between the STFT time frames is calculated through the multiplication of the transposed $\mathbf{V}$ by $\mathbf{V}$ with the normalization of the $\mathbf{V}$. This is shown in Eq. 2.

$$S(k_a,\mathrm{k}_b) = \frac{\sum_{\mathrm{i}=1}^{n} V(\mathrm{i},\mathrm{k}_a)V(\mathrm{i},\mathrm{k}_b)}{\sqrt{\sum_{\mathrm{i}=1}^{n} V(\mathrm{i},\mathrm{k}_a)^2}\sqrt{\sum_{\mathrm{i}=1}^{n} V(\mathrm{i},\mathrm{k}_b)^2}}, \tag{2}$$

Zahra Zali 28.11.2022 14:10
Deleted: of

Zahra Zali 28.11.2022 14:10
Deleted: is

Zahra Zali 28.11.2022 14:12
Deleted: originated

Zahra Zali 24.11.2022 09:46
Deleted: most of

Zahra Zali 24.11.2022 09:44
Deleted: dominantly

Zahra Zali 24.11.2022 09:49
Deleted: signals and can be considered to have a monochromatic or harmonic appearance in the spectrogram

Zahra Zali 28.11.2022 08:28
Deleted: region

Zahra Zali 28.11.2022 08:28
Deleted: region

Zahra Zali 28.11.2022 08:28
Deleted: region

Zahra Zali 28.11.2022 08:28
Deleted: region

Zahra Zali 28.11.2022 08:29
Deleted: region

Zahra Zali 24.11.2022 22:10
Deleted: In the second step

Zahra Zali 24.11.2022 22:11
Deleted: the specified frequency range containing

Zahra Zali 28.11.2022 14:18
Deleted:

Zahra Zali 24.11.2022 22:12
Deleted: previously

where **S** is the similarity matrix. Each point (k_a, k_b) in **S** is the cosine similarity between time frame k_a and k_b of **V**, $\forall k_{a,b} \in [1,\mathrm{m}]$, where *m* is the number of time frames and *n* is the number of frequency channels for each time frame. Once the similarity matrix is calculated we use it to determine the most similar time frames to each single time frame. For time frame k_a we compare all the values in $S(k_a, \mathrm{k}_i)$ for i∈ [1,m]. We identify similar frames for time frame k_a, by choosing the upper 2% of the all time frames with the highest similarities.

Finally, all similar time frames to any frame *k* in **V** are stored in a temporary array ***K***. Those similar time frames are used to create a repeating spectrogram model **W**. The corresponding frame in **W** is obtained by taking the median of ***K*** for each frequency at each time frame *k*. Those time-frequency bins, which are similar with little deviations between repeating frames, are captured by the median and constitute the repeating spectrogram model. This spectrogram contains only similar and repeating patterns. The time-frequency bins with large deviations between repeating frames would constitute nonrepeating transient patterns and would be suppressed by median filtering.

The nonnegative spectrogram **V** is the sum of two nonnegative spectrograms of repeating and nonrepeating patterns, hence, **W** (the repeating spectrogram model) should always have smaller values or at most be equal compared to **V**. To ensure this, a repeating spectrogram model $\widetilde{\mathbf{W}}$ is defined by taking the minimum between **W** and **V**. The nonrepeating spectrogram model is derived by subtracting $\widetilde{\mathbf{W}}$ from **V**.

We use these two (the repeating and the nonrepeating) spectrogram models to create two time-frequency masks for repeating and nonrepeating patterns, respectively. Instead of the binary mask, which is used in Rafii & Pardo (2012), we use soft masks via Wiener filtering (Vaseghi, 1996). The calculation of the soft masks is shown in the following equations:

$$M1 = \frac{\widetilde{W}^2}{\widetilde{W}^2 + \left(V - \widetilde{W}\right)^2}, \tag{3}$$

$$M2 = \frac{\left(V - \widetilde{W}\right)^2}{\left(V - \widetilde{W}\right)^2 + \widetilde{W}^2}, \tag{4}$$

in which **M1** and **M2** are repeating and nonrepeating masks respectively. We multiply the masks with the input amplitude spectrogram **V** to separate the repeating and nonrepeating components. The element-wise multiplication of the masks by the input amplitude spectrogram **V** is shown in the following equations:

Zahra Zali 25.11.2022 08:57
Deleted: , which have

Zahra Zali 28.11.2022 08:30
Deleted: S values

Zahra Zali 25.11.2022 08:57
Deleted: , are identified as similar frames for time frame

Zahra Zali 28.11.2022 14:19
Deleted: the

$$R = M1 \otimes V, \quad (5)$$

$$NR = M2 \otimes V, \quad (6)$$

in which **R** and **NR** denote repeating and nonrepeating amplitude spectrograms respectively.

The resulting **R** and **NR** spectrograms are shown in Fig. 2a for a specific/typical example of an OBS recording. As can be observed in the **R** spectrogram, in particular the low frequency harmonic or monochromatic signals below 0.1 Hz are well captured. We applied the SIM algorithm only to the frequency band below 0.1 Hz and above 1 Hz. In the frequency band from 0.1 Hz to 1 Hz the signals remain unchanged by this procedure. This is the first constraint we consider for the SIM algorithm. In the field of noise reduction using signal processing techniques, a very important point is to not modify the signals of interest for analysis. P and S waveforms in the teleseismic earthquake signals have often frequency content in the range of 0.1 Hz to 1 Hz with a dominant frequency around 0.3 Hz. Oceanic microseism noise, which is usually present in the OBS data, has a dominant frequency around 0.1 Hz to 0.3 Hz. As P and S phases have similar dominant frequency as the microseism noise wavefield, superposition of both wavefields could happen in this frequency range. They could interfere constructively or destructively so the resulting amplitude could be higher or lower compared to the original P or S phase amplitudes. Considering these interferences, using the SIM algorithm, may result in creating fake higher amplitude for these phases or losing part of their amplitude in the noise reduced signal. But this could be problematic only when the amplitude of the noise is changing over the time. For a noise signal with almost constant amplitude, the SIM algorithm can extract the true amplitude of the noise even in the interference moments. However, the microseism noise has slightly varying amplitude over time.

Before moving to the second step we introduce a second constraint parameter, which we use in the SIM algorithm. Surface waves of teleseismic events show usually a dispersed narrow-band signal and correspond to mainly horizontal patterns of short duration (on a daily scale) in the spectrogram. Given the way the HPS is separating harmonic from transient signals, the surface wavetrain may be erroneously recognized as harmonic component and thus be separated as noise signal. In order to prevent this and preserve the whole frequency content of the earthquake, we define a so-called waiting factor for the similarity calculation introducing a minimum time distance between two consecutive similar frames. For the problem of retaining teleseismic surface waves we found that a waiting time of at least two hours prevents the algorithm to prune surface waves from the transient signal part. The rationale is that the duration of a teleseismic event is usually less than two hours whereas the noise components have longer duration. Using this waiting factor prevents separating any harmonic component of the earthquake signal as noise component. As a side effect this constraint causes that short-duration harmonic/monochromatic noise signals won't be well captured, too. However, these types of signals are not common in OBS data (see the

Zahra Zali 28.11.2022 14:20
Deleted: s

Zahra Zali 24.11.2022 22:22
Deleted: The reason is related to the frequency content of the noise and earthquake signals and how the SIM algorithm separates them.

Zahra Zali 28.11.2022 14:20
Deleted: (on a daily scale) short duration

Zahra Zali 28.11.2022 14:21
Deleted:

Sect. 2).

In the second step of our algorithm, to target noise signals in the frequency range of 0.1 Hz to 1 Hz, we use MED as it is described in the Sect. 3.2. We apply this second part of the noise removal procedure only to a restricted frequency band of 0.1 Hz to 1 Hz. The dominant noise in the mentioned frequency range is the current-induced harmonic tremor signal (see the Sect. 2).

First we create the $\mathbf{X}'$ spectrogram which is equal to **X** in the mentioned frequency range and is equal to zero outside of this band. Then we apply a horizontal median filter to $\mathbf{X}'$ in order to separate harmonic components. This results in the harmonic spectrogram **H,** which contains near-horizontal patterns captured by the median filter.

Now we have two separated spectrograms for noise signals: **R**, which is derived from the first step, and **H**, which is derived from the second step. Summing these two spectrograms will build the noise spectrogram **N**. Subtracting **N** from the input amplitude spectrogram **V** will construct the transient spectrogram **T**.

As can be seen in Fig. 2a in step 2, the dominant energy of the narrow-band signals with gliding frequencies in the range of 0.1 Hz to 1 Hz (the current-induced harmonic tremor noise as introduced in the Sect. 2) is captured in the noise spectrogram **N**, but part of it remains in the transient spectrogram **T**. Signals with changing frequency which don't form complete horizontal lines in the spectrogram, are difficult to capture by our HPS algorithm, so part of their energy remains in the final spectrogram.

3.5 Reconstruction of the denoised signal

In order to reconstruct the noise-removed signal in the time domain we must add phase information to the spectrogram. We had separated the complex-valued spectrogram **X** into its amplitude **V** and its phase component using Eq. 1 and all the further modifications have been applied to the amplitude spectrogram **V**. The phase of input signal SO is mostly affected by the phase of noise signals as they have the dominant energy in the signal. Therefore, we use the phase information of SO in order to reconstruct the noise signal. We add this phase to the noise spectrogram **N** using the following equation:

$$N' = N * exp(1j * \varphi), \tag{7}$$

where N' is the complex-valued noise spectrogram. We reconstruct the noise signal *NS* from the complex spectrogram N', using the inverse STFT. Finally the OBS denoised signal HPS (HPS here represents the SO signal after the HPS processing) is obtained by subtracting the noise signal from the input OBS signal SO using the following equation:

Zahra Zali 24.11.2022 22:40
Deleted: We don't apply MED for the frequency range below 0.1 Hz to avoid an interference with the surface wave signals of teleseismic events that shall be retained.

Zahra Zali 28.11.2022 14:18
Deleted:

Zahra Zali 24.11.2022 10:07
Deleted: is applied

Zahra Zali 24.11.2022 10:08
Deleted: N

Zahra Zali 24.11.2022 10:09
Deleted:

Zahra Zali 24.11.2022 10:08
Deleted: will be

Zahra Zali 24.11.2022 10:08
Deleted: and will be separated in the harmonic spectrogram **H.**

Zahra Zali 28.11.2022 14:18
Deleted:

Zahra Zali 24.11.2022 09:06
Deleted: that is still

Zahra Zali 24.11.2022 09:06
Deleted: ed

Zahra Zali 24.11.2022 09:11
Deleted: The

Zahra Zali 24.11.2022 09:11
Deleted: s

Zahra Zali 24.11.2022 09:11
Deleted: that

Zahra Zali 24.11.2022 09:12
Deleted: be

Zahra Zali 24.11.2022 09:12
Deleted: d

$$HPS = SO - NS, \quad (8)$$

3.6 Parameters selection

Many typical noise signals observed in OBS recordings are harmonic, monochromatic or narrow-band signals with gliding frequencies (see the Sect. 2). In order to extract the expected narrowband noise signals from the STFT we require a high frequency resolution in the spectral domain, therefore, making it necessary to use sufficiently long time windows for the spectral analysis. Here we use an FFT window length of 163.84 seconds with an overlap of 75%, corresponding to an FFT size of 16384 at a sampling frequency of 100 Hz, which corresponds to a frequency resolution of 0.006 Hz.

We use a kernel size of 80 for the median filter in the MED algorithm. The larger the kernel size, the more noise signal would be captured. However, using very large sizes could introduce waveform distortions. As it is discussed in Driedger et al. (2021), the kernel size is not critical as far as not using extreme values. Our tests show that a kernel size of 80 is the largest size, which leads to a safe separation without capturing any energy of the teleseismic signal.

The values of parameters, which we used for this study, are presented in the Table 1. These are our recommendations for noise reduction of teleseismic earthquakes. One can tune the parameters based on other specific applications such as denoising local earthquakes or extracting specific signals like microseism signal.

4 Results and Discussion

4.1 General Results

In this section we aim to demonstrate the reliability of our HPS noise reduction algorithm and evaluate the improvement of the OBS data. We applied the method to synthetic and real teleseismic earthquake data recorded by the OBS station D10 of the DOCTAR array (e.g., Hannemann et al, 2016, Hannemann et al., 2017). The synthetics were calculated for a source-receiver epicentral distance of 40° (focal depth: 45 km, focal mechanism: double couple, source duration: 4 s) by using the full wavefield software qseis (Wang, 1999) and a modified average ak135 velocity model including a water layer (Kennett et al, 1995). The crustal structure of the velocity model is adapted to the oceanic crust (crustal thickness is 6.6 km) in that area and the water depth is fixed to 4.9 km. Real oceanic noise of the ZRT components recorded by the station D10 is added to the corresponding components of the synthetic teleseismic signal. We created synthetics for three different noise situations at the beginning (N1), during (N2) and after (N3) tidal currents (Fig. 3) each with theoretical SNR of 1–10 between noise and P-onset on pure synthetic Z. Throughout the whole paper the SNR is defined as root mean square (RMS) of the signal divided by RMS

Zahra Zali 28.11.2022 14:23
Deleted: at

Zahra Zali 28.11.2022 14:23
Deleted:

Zahra Zali 25.11.2022 08:02
Deleted: standard

Zahra Zali 25.11.2022 08:13
Deleted: earthquake

Zahra Zali 28.11.2022 14:25
Deleted: prove

Zahra Zali 24.11.2022 11:53
Deleted: 11.5 km deep

Zahra Zali 25.11.2022 14:59
Deleted: 5

Zahra Zali 24.11.2022 12:30
Deleted: scenarios

of the noise. For further details of synthetic data creation see Fig. S2. For the comparison with real data, we selected in total 46 teleseismic events with magnitudes Mw >5.6 and epicentral distances of 30–160° (see Fig. S1). Here only those events were used, where a P onset could be visually identified. The pre-selection of the events is taken from Hannemann et al. (2017) and expanded by some events with low magnitudes (see Table S1). In the following, we will discuss the improvement of the records by comparing the seismograms and spectrograms of synthetic and real data. We also illustrate the improvement for two seismological applications (teleseismic surface wave group velocity analysis and receiver function analysis). For some observations, e.g. checking the phase arrival of the teleseismic body waves, we rotated the arbitrarily orientated horizontal components of the real data into the ZRT system. The orientation angles are taken from the previous study on the DOCTAR array (Hannemann et al., 2016).

Comparing the spectrograms and waveforms of the synthetic example we see a significant improvement of SNR in the HPS processed data set on all components (e.g. Fig. 3 and Fig. S3–5 for the real data). The continuous spectral lines of the assumed electronic noise are removed from the data, as well as most of the spectral lines related to tremor episodes of head-buoy strumming. During the tides, we observe a reduction of the spectral amplitudes for the tilt noise, as well as for the general background noise (Fig. 3 and Fig. S3–5) on the horizontal components. The results concluded from the spectrograms are confirmed by the spectra (Fig. 2b), which show the removal of the spectral peaks of the electronic noise (0.05, 0.1, 0.15 Hz) and the tremor episodes (0.5–1 Hz). The whole amplitude and the phase information of the synthetic earthquake are preserved in the HPS signal (see Fig. 3).

To quantify the improvements obtained when using our method, we calculated the cross-correlation of the teleseismic waveform, the SNR of the teleseismic body-wave phases and the RMS of the teleseismic waveform before and after denoising. Because most of the oceanic noise ranges at frequencies below 1 Hz, which is also the most interested frequency range of the OBS analysis, a 1 Hz low pass filter is applied to the signals before all result calculations.

We calculated the correlation coefficient for synthetic SO and HPS compared with the synthetic earthquake signal for different SNR and noise realizations and plotted it in Fig. 4a. The high correlation coefficients for HPS and synthetic compared with SO and synthetic in all cases demonstrate a significant noise reduction. Furthermore, it is an indication that the HPS denoising preserves the earthquake signal and doesn't introduce significant waveform distortions since the HPS is more similar to the synthetics compared to SO. In the following we show other measures that confirm the preservation of the earthquake signal.

For the SNR calculation we used a signal window of 30 s starting from the theoretical onset (direct P on Z component, direct S on R and T component and Love wave on the T component) and a noise window of 60 s starting 70 s before the theoretical onset. For the Love wave, the SV phase (R component) and P phase (Z component) the SNR increased significantly (Fig. 4b). We find that the noise type properties influence the perceived SNR improvement. It appears that there is no SNR improvement on the T-component for Noise situation N1 (Fig. 4b, the second panel). N1 is taken from the tidal current event's beginning, where there is

Zahra Zali 28.11.2022 14:27
Deleted: and confirm it with real data

Zahra Zali 28.11.2022 14:26
Deleted: verify

Zahra Zali 24.11.2022 17:12
Deleted: the

Zahra Zali 24.11.2022 12:59
Deleted: is seen

Zahra Zali 24.11.2022 13:00
Deleted: The amplitudes of the frequencies corresponding to the teleseismic event and its waveforms are maintained

Zahra Zali 28.11.2022 08:16
Deleted: improvements

Zahra Zali 24.11.2022 12:02
Deleted: of

Zahra Zali 24.11.2022 12:03
Deleted: the

a significant variation in noise-frequencies over time. In this instance, the signal and noise have comparable frequency ranges. Despite the SNR showing no increase, a visual check of the matching trace reveals a definite improvement in the waveform for the SH-wave on the T component. The results from the cross-correlation (Fig. 4a), confirm the improvement and preservation of the waveform. The SNR should not be utilized alone to assess the improvement by HPS noise reduction approach since we are concentrating on the preservation of the waveform and the SNR comparison strongly depends on the noise situation. The improvement of the traces by the HPS noise reduction approach is confirmed by the study of the cross-correlations, RMS (which is explained in the following paragraph), and the pure waveforms, even though the SNR is not improving in all instances.

The RMS amplitudes of a noise-free R component synthetic, SO and HPS signals are estimated over 8 seconds windows with 80% overlap and plotted in Fig. 4c. Comparing the RMS amplitude of the synthetic, SO and HPS we see that the synthetic and HPS have similar amplitude ranges while SO has a much higher amplitude. This shows a significant noise reduction in HPS along with preserving the energy of earthquake and all the phase arrivals. As there is some noise remaining after denoising we see some differences in the overall shapes of the RMS amplitude of the synthetic and HPS (especially after minute 24 which is almost at the end of the energy of the synthetic signal). However, HPS shows peaks on the arrival times of seismic phases of the synthetic which means that the energy of seismic phases is preserved after denoising. The minor changes in seismic phase shapes of the synthetic and HPS are also due to the remaining noise. The seismograms and spectrograms related to this example are presented in Fig. 3. Figure 4d shows a comparison of RMS amplitude of the original noise in SO (blue curve), the remaining noise in HPS after denoising (red curve) and the synthetic earthquake (green curve) signals. Besides a high noise reduction in HPS, the plot shows that the remaining noise is independent of the pattern of the synthetic earthquake, which confirms that the denoising process doesn't affect the earthquake energy in the HPS signal.

Zahra Zali 24.11.2022 17:21
Deleted: For SH phase on T component we observe a few apparent SNR decreases comparing SO with HPS traces (Fig. 4b). The SNR is calculated on the noise contaminated SO traces, it hence compares noise with noise contaminated synthetic signal. Because of this and because we added the synthetics amplified according to SNR for P-arrival on Z component to the real noise, in a few cases we observe apparent SNRs slightly below 1 for a few SH phases (see Fig. 4b).

Zahra Zali 28.11.2022 14:29
Deleted:

Zahra Zali 24.11.2022 13:12
Deleted: energy

Zahra Zali 28.11.2022 14:29
Deleted: ,

Zahra Zali 28.11.2022 14:29
Deleted: h

Zahra Zali 28.11.2022 14:29
Deleted: is

Zahra Zali 28.11.2022 14:30
Deleted: from

4.2 Applications

By applying our HPS noise reduction algorithm, we aim to improve seismological analysies, especially those involving the analysis of teleseismic body and surface waves. Valuable constraints of the Earth's structure in oceanic regions can be taken from the analysis of the SH-wavefield like Love-waves, which are not influenced by the water column, but often cannot be analyzed due to strong noise on the horizontal components. SV waves are also often masked by noise, but are for instance important for tomography studies or S and SKS shear wave splitting analysis (e.g. Silver and Chan, 1991). Other techniques using the SV-wavefield like the Z/R ratio of the teleseismic Rayleigh waves (Tanimoto & Rivera, 2008), or receiver functions (RF) (Langston, 1979) also rely on clear radial component readings. In the following we will show the improvement which was achieved for the SH arrivals and for the group velocity analysis of teleseismic Rayleigh- and Love waves, as well as for the receiver function analysis.

4.2.1 SH-waves

Since SH-waves are weak in energy and displayed on the noise-contaminated transversal horizontal component (T), they are sparsely observable on OBS recordings and are mostly masked by the high noise level. However, on the HPS processed data we see an improvement of the SNR on the T-component (see Fig. 4b). In many cases the SH-phase is clearly identifiable on the HPS T-component (see Fig. 3d for a synthetic data and Fig. S6 for a real data example).

4.2.2 Surface waves

Rayleigh waves in deep oceanic domains are strongly influenced by the water column, because most of the wave energy is traveling in the water. This poses a problem if the water depth changes along the travel path. Love waves are not influenced by the water column but are recorded only on horizontal components and their recordings on OBS systems are therefore more disturbed by strong noise sources like tilt-inducing tidal currents. To test the performance of the HPS noise reduction algorithm in the long period range, we performed a measurement of group velocities of Love and Rayleigh waves with the Multiple Filter Technique (MFT) (Dziewonski et al., 1969). Figure 5 shows group velocity curves for the synthetic Love wavetrain for the three noise situations N1-N3. For the MFT analysis we used the software mft96 (Herrmann, 2013). The unfiltered seismograms in the top panels (Fig. 5a–c) correspond to the P-wave SNR = 1 scenario. In all three cases the clarity of the dispersion curve is greatly enhanced in the images resulting from the HPS processed traces (Fig. 5e–g) in comparison to the noise free image (Fig. 5d). Also the seismogram traces improved greatly. The dispersion maps show that also noise energy in the range of the signal frequencies is removed successfully in the frequency range 0.05 to 0.2 Hz. Longer signal periods which are weakly visible in the noise-free image (Fig. 5d) can not be recovered. The corresponding results for the Rayleigh wavetrain on the radial component are shown in Fig. S7. For the N3 case here also longer periods down to 40 s can be successfully denoised.

For an evaluation of the HPS denoising technique on real surface wave data we selected 23 events with magnitudes larger than Mw 6.0 in the distance range between 47.5° and 159.6° and added one event with Mw= 5.6 at a distance of 37.9° (see Fig. S1). Figure S8 shows seismograms and MFT analysis examples for three events with different magnitudes and in different distances. The resulting group velocity dispersion curves for all 24 events for the original and processed data are shown in Fig. S9. For all components we find that the improved signal to noise ratio of the processed data allows the analysis of more events and of a broader period range than in the original data.

4.2.3 Receiver Functions

Receiver functions have been proven to be a valuable tool to observe the Earth's structure using teleseismic events (e.g., Langston, 1979, Ammon et al., 1995, Kind et al., 1995; Rondenay, 2009). Separating the source site from the receiver site by deconvolution allows to estimate the Earth's structure beneath the station. Here, we compare the receiver functions calculated from the synthetic examples and from real data before and after denoising (Fig. 6). The synthetics used for the receiver function calculation are pure

Zahra Zali 28.11.2022 14:30
Deleted: data

Zahra Zali 28.11.2022 14:30
Deleted: disappeared behind

Zahra Zali 28.11.2022 14:31
Deleted:

Zahra Zali 24.11.2022 12:27
Deleted: Group velocity curves are for instance used as input data for tomographic studies to reveal the 3D structure of the lithosphere and upper mantle.

synthetic signals contaminated by real noise (N1, N2, N3). On the synthetics, the SNR for P ranges between 1–10 (for detailed description of the synthetic creation, see Sect. 4.1, Fig. 3 and S2). Receiver function analysis and the observation of the Earth's structure beneath the DOCTAR array was already calculated by Hannemann et al. (2017). Here, we don't aim to estimate the crustal and mantle structures, instead we aim to compare the P-receiver Functions of the radial component calculated from the original synthetic and real data (SO R-RF) with receiver functions of the radial component from the HPS processed synthetic and real data (HPS R-RF). To calculate the receiver functions, we applied the iterative deconvolution in the time domain (Ligorría & Ammon, 1999). We corrected the data for the Ps-phase, quality controlled (e.g. P-onset at 0 s on Z of HPS R-RF), stacked and low-pass filtered the synthetic data at 2 Hz and bandpass filtered the traces between 0.05–0.5 Hz for the real data with a zero-phase Butterworth filter. For both synthetic and real receiver function, the noise level strongly decreased and we observe a significant decrease in variance on the HPS traces compared to the SO traces (Fig. 6).

Our result shows that determination of the crustal- and mantle-phases is more reliable on the HPS R-RF stack than on the SO R-RF stack for both synthetic and real data (Fig. 6). We observe more distinct Ps-phase arrivals on the HPS R-RF than on the SO R-RF stack. The Ps-phases are caused by the P-to-S conversion at the Mohorovičić-, 410-km and 660-km discontinuity (hereafter referred to as Moho, 410, and 660, respectively; e.g. Deuss, 2009). For the synthetic example, we expect the P-to-s conversion at the Moho at depths of 11.5 km to arrive at 0.8s, which is better resolved in the synthetic HPS R-RF than in the synthetic SO R-RF, same for it's multiple (P_MsPp) and the water multiples every 6.5s (M_{WATER}, Fig. 6a).

Assuming ak135 velocities we would expect the $P_{410}s$-phase (Ps conversion at the 410) to arrive at around 43 s and the $P_{660}s$-phase (Ps conversion at the 660) at around 66.8 s delayed to the direct P-arrival (see Fig. 6 a & b).

Instead of a rather weak peak on the SO-R-RF real data stack we observe a strong peak at around 43 s, with a good SNR on the HPS R-RF stack, indicating the sharp velocity contrast at the 410 (Fig. 6b). Comparing SO-RF and HPS-RF real data stacks, the amplitudes of the P660s-phase on the HPS decreased and became a broader peak. This aligns with our expectations from a conversion at a gradual velocity contrast as at the 660. These results are in line with the analysis of the crustal and mantle structure beneath the DOCTAR array presented by Hannemann et al. (2017). The negative phase (X1 in Fig. 6b) arriving at around 5 s is stronger on the HPS-R-RF real data stack than on the SO-R-RF real data stack and might either indicate the PpSs multiple of the Ps-phase at the Moho, or the direct P-to-s conversion at the LAB. On the HPS-R-RF real data stack we observe a strong positive phase (X2) arriving at 12 s (Fig. 6b). This phase has not been identified by Hannemann et al. (2017) and a detailed analysis of its origin is beyond the scope of this study, but it might be related to the water multiples.

5 Conclusions

Zahra Zali 25.11.2022 15:49

Deleted: Comparing the SO-RF and the HPS-RF real data stacks, the amplitudes of the P660s-phase decreased and became a broader peak, which we would expect from a conversion at a more gradual velocity contrast at the 660 (Fig. 6b).

Zahra Zali 25.11.2022 15:35

Deleted: In general, receiver functions of OBS data are difficult to analyze and although the SNR of the HPS processed data has been improved, the analysis of the real data is still difficult, especially compared to receiver functions from land stations.

In this work we have developed a method to separate the signals of teleseismic earthquakes from other signals in OBS recordings resulting in noise reduction of OBS data. Our method is a combination of two HPS algorithms from the field of MIR to separate harmonic and percussive components of OBS data. Earthquake signals as percussive components are separated from noise signals as harmonic components. The noise signal is reconstructed using the phase information of the original signal. Subtracting the noise signal from the original signal derives the noise-reduced signal. Our two-step HPS approach results in a cleaner, noise-reduced signal where the teleseismic broadband earthquake waveforms are preserved with their whole frequency content. Our synthetic tests shows that the SNR of HPS noise reduced signal significantly increases in most cases, however, the apparent SNR improvement depends on the noise type characteristics. The type of noise signals, which are eligible for our noise reduction algorithm contains most of the OBS noise energy.

The extracted noise signal contains some different signals where each can be derived by applying a band pass filter to the extracted noise signal in a proper frequency band. The derived signal may be used in researches related to that signal. For example the microseism signal can be extracted and used for investigation of the source generation area of microseisms.

From our analysis of the broadband seismograms, we find out that the improvement is significant and allows a broader and more reliable analysis of teleseismic earthquake data. Applications like the receiver function technique and SH-wave and Love wave analysis are considerably improved after applying the HPS noise reduction algorithm.

Group velocity analysis of teleseismic surface wavetrains showed that application of the HPS noise reduction technique allows to analyze more events and to analyze them in a broader frequency range. Especially more and wider Love wave dispersion curves could be recovered. The noise reduction algorithm improves the horizontal components significantly, which allows the OBS community to apply a broader range of seismological methodologies, including the horizontal components, to the OBS-data.

In conclusion, the presented method is a powerful algorithm for separation and extraction of different signals from OBS data and has especially application in noise reduction of OBS signals.

Code and data availability

A Python package named NoiseCut (Zali, 2022) and the code related to the proposed method along with an example of real data is freely available from https://github.com/ZahraZali/NoiseCut. The average computation time for this example (one day OBS signal with a sampling frequency of 100 Hz) is about 7 minutes on a PC with an Intel core i7 (six-core) processor of 2.2 GHz and 16 GB of RAM. A Jupyter notebook with all the Python codes and parameters related to the proposed method is available as an electronic supplement. The sea floor seismological data were archived by Alfred Wegener Institute (AWI), Helmholtz Centre for Polar Research, Bremerhaven, Germany, and are available upon request. The supplementary material related to this article contains list of all earthquakes used in this study and a map showing their location. The illustrations of the semi-synthetic data generation are presented in the

Zahra Zali 28.11.2022 14:32
Deleted: the

Zahra Zali 28.11.2022 14:32
Deleted: data

Zahra Zali 28.11.2022 14:32
Deleted: ed

Zahra Zali 28.11.2022 14:32
Deleted: an

Zahra Zali 24.11.2022 16:13
Deleted: We discussed the motivation of using a

Zahra Zali 24.11.2022 16:13
Deleted:

Zahra Zali 24.11.2022 16:13
Deleted: , that

Zahra Zali 24.11.2022 16:44
Deleted: We also discussed

Zahra Zali 24.11.2022 16:14
Deleted: t

Zahra Zali 24.11.2022 16:14
Deleted: that

Zahra Zali 24.11.2022 16:55
Deleted: . ... [3]

Zahra Zali 24.11.2022 16:49
Deleted: may

Zahra Zali 24.11.2022 16:54
Deleted: For the receiver function, we could observe a more distinct phase for the P-to-S conversion at the Moho for the synthetic case and at the 410 km discontinuity for the real data.

supplementary material as well. An example of three components seismogram and spectrogram before and after applying HPS noise reduction algorithm to real data, Rayleigh wave group velocity analysis for a synthetic example, MFT analysis for three real events and group velocity curves for some real events are also presented through figures in the supplementary material.

Author contribution

Z.Z. developed the algorithm and designed the study. T.R. created the synthetics data, conducted the synthetic tests, and measured the receiver functions. F.K. conducted the group velocity analysis. Z.Z., T.R., and F.K. evaluated the results. Z.Z. and T.R. wrote the initial draft. All authors wrote the final manuscript and discussed the results.

Competing interests

The authors declare that they have no conflict of interest.

Acknowledgments

Zahra Zali is grateful for the support by the German Academic Exchange Service (DAAD) through the Graduate School Scholarship Programme under reference number 91721165. This work was also supported by the German Research Foundation (DFG MU 2686/13-1, SCHE 280/20-1) and the Daimler Benz Foundation (32-02/18). The sea floor seismological data were archived by Alfred Wegener Institute (AWI), Helmholtz Centre for Polar Research, Bremerhaven, Germany, and are available upon request. We acknowledge the DEutscher Geräte-Pool für Amphibische Seismologie (DEPAS) pool (Alfred-Wegener-Institut Helmholtz-Zentrum für Polar- und Meeresforschung et al., 2017) that is currently the largest European OBS pool. We acknowledge Sebastian Heimann for helping in packaging of the code related to the method. For building our method, we used Librosa, a Python package for audio and music signal processing (McFee et al., 2020). The data processing was done using obspy (Beyreuther et al., 2010) and pyrocko (Heimann et al., 2017); the receiver functions were calculated using the rf-package (Eulenfeld, 2020).

References

Alfred-Wegener-Institut, Helmholtz-Zentrum für Polar- und Meeresforschung et al.: DEPAS (Deutscher Geräte-Pool für amphibische Seismologie): German Instrument Pool for Amphibian Seismology, J. Largescale Res. Facil., 3, A122, https://doi.org/10.17815/jlsrf-3-165, 2017.

Ammon, C. J., Randall, G. E., & Zandt, G.: On the nonuniqueness of receiver function inversions, J. Geophys. Res.-Sol. Ea., 95(B10), 15303-15318, https://doi.org/10.1029/JB095iB10p15303, 1990.

Zahra Zali 24.11.2022 17:42
Deleted: Journal of largescale research facilities, 3, A122,

An, C., Cai, C., Zhou, L., & Yang, T.: Characteristics of Low-Frequency Horizontal Noise of Ocean-Bottom Seismic Data, Seismol. Res. Lett., https://doi.org/10.1785/0220200349, 2021.

Bell, S. W., Forsyth, D. W., & Ruan, Y.: Removing noise from the vertical component records of ocean-bottom seismometers: Results from year one of the Cascadia Initiative, B. Seismol. Soc. Am., 105(1), 300-313, https://doi.org/10.1785/0120140054, 2015.

Beyreuther, M., Barsch, R., Krischer, L., Megies, T., Behr, Y., Wassermann, J.: ObsPy: A Python Toolbox for Seismology. Seismol. Res. Lett., 81(3), 530-533, 2010.

Brink, K. H.: Tidal and lower frequency currents above Fieberling Guyot. J. Geophys. Res.-: Oceans, 100(C6), 10817-10832, https://doi.org/10.1029/95JC00998, 1995.

Corela, C.: Ocean bottom seismic noise: applications for the crust knowledge, interaction ocean-atmosphere and instrumental behaviour. Ph.D. thesis, University of Lisbon, 339 pp, 2014.

Crawford, W. C.: Determination of oceanic crustal shear velocity structure from seafloor compliance measurements (Doctoral dissertation, University of California, San Diego), 1994.

Crawford, W. C., & Webb, S. C.: Identifying and removing tilt noise from low-frequency (< 0.1 Hz) seafloor vertical seismic data. B. Seismol. Soc. Am., 90(4), 952-963, https://doi.org/10.1785/0119990121, 2000.

Crawford, W. C., Webb, S. C., & Hildebrand, J. A.: Estimating shear velocities in the oceanic crust from compliance measurements by two-dimensional finite difference modeling. J. Geophys. Res.-Sol. Ea., 103(B5), 9895-9916, https://doi.org/10.1029/97JB03532, 1998.

Deuss, A.: Global observations of mantle discontinuities using SS and PP precursors. Surv. Geophys., 30(4-5), 301-326, https://doi.org/10.1007/s10712-009-9078-y, 2009.

Driedger, Jonathan, Meinard Müller, and Sascha Disch. "Extending Harmonic-Percussive Separation of Audio Signals." In ISMIR, pp. 611-616. 2014.

Duennebier, F. K., & Sutton, G. H.: Fidelity of ocean bottom seismic observations, Oceanographic Literature Review, 10(43), 996, https://doi.org/10.1007/BF01204343, 1995.

Dziewonski, A., S. Bloch, and M. Landisman.: A technique for the analysis of transient seismic signals, B. Seismol. Soc. Am., 59, no. 1, 427-444, https://doi.org/10.1785/BSSA0590010427, 1969.

Essing, D., Schlindwein, V., Schmidt-Aursch, M. C., Hadziioannou, C., & Stähler, S. C.: Characteristics of Current-Induced Harmonic Tremor Signals in Ocean-Bottom Seismometer Records, Seismol. Res. Lett., 92(5), 3100-3112. , https://doi.org/10.1785/0220200397, 2021.

Eulenfeld, T.: rf: Receiver function calculation in seismology, Journal of Open Source Software, 5(48), 1808, https://doi.org/10.21105/joss.01808, 2020.

Fitzgerald, D.: Harmonic/percussive separation using median filtering, In Proceedings of the International Conference on Digital Audio Effects (DAFx) (Vol. 13), 2010.

FitzGerald, D.: Vocal separation using nearest neighbours and median filtering, 23rd IET Irish Signals and Systems Conference, Maynooth. 28-29th. June 2012, https://doi.org/10.1049/ic.2012.0225, 2012.

Friedrich, A., Krüger, F., & Klinge, K.: Ocean-generated microseismic noise located with the Gräfenberg array, J. Seismol., 2(1), 47-64, https://doi.org/10.1023/A:1009788904007, 1998.

Gaspà Rebull, O., Cusí, J. D., Ruiz Fernández, M., & Muset, J. G.: Tracking fin whale calls offshore the Galicia Margin, north east Atlantic Ocean, The Journal of the Acoustical Society of America, 120(4), 2077-2085, https://doi.org/10.1121/1.2336751, 2006.

Griffin, O. M.: Vortex-Induced Vibrations of Marine Cables and Structures, NRL Memorandum Report 5600, Naval Research Laboratory – Marine Technology Division, Washington D.C, 1985.

Hannemann, K., Krüger, F., Dahm, T., & Lange, D.: Structure of the oceanic lithosphere and upper mantle north of the Gloria fault in the eastern mid-Atlantic by receiver function analysis, J. Geophys. Res-Sol Ea., 122(10), 7927-7950, https://doi.org/10.1002/2016JB013582, 2017.

Hasselmann, K.: A statistical analysis of the generation of microseisms. Rev. Geophys., 1(2), 177-210, https://doi.org/10.1029/RG001i002p00177, 1963.

Heimann, S., Kriegerowski, M., Isken, M., Cesca, S., Daout, S., Grigoli, F., Juretzek, C., Megies, T., Nooshiri, N., Steinberg, A., Sudhaus, H., Vasyura-Bathke, H., Willey, T., Dahm, T.: Pyrocko - An open-source seismology toolbox and library. V. 0.3. GFZ Data Services, https://doi.org/10.5880/GFZ.2.1.2017.001, 2017.

Herrmann, R. B.: Computer programs in seismology: An evolving tool for instruction and research, Seism. Res. Lettr., 84, 1081-1088, https://doi.org/10.1785/0220110096, 2013.

Zahra Zali 24.11.2022 18:04
Deleted: Seismological Society of America

Janiszewski, H. A., Gaherty, J. B., Abers, G. A., Gao, H., & Eilon, Z. C.: Amphibious surface-wave phase-velocity measurements of the Cascadia subduction zone. Geophys. J. Int., 217(3), 1929-1948, https://doi.org/10.1093/gji/ggz051, 2019.

Johnson, J. B., & Watson, L. M.: Monitoring volcanic craters with infrasound "music", Eos, 100. https://doi.org/10.1029/2019EO123979, 2019.

Kennett, B. L., Engdahl, E. R., & Buland, R.: Constraints on seismic velocities in the Earth from traveltimes. Geophys. J. Int., 122(1), 108-124, https://doi.org/10.1111/j.1365-246X.1995.tb03540.x, 1995.

Kind, R., Kosarev, G. L., & Petersen, N. V.: Receiver functions at the stations of the German Regional Seismic Network (GRSN). Geophys. J. Int., 121(1), 191-202, https://doi.org/10.1111/j.1365-246X.1995.tb03520.x, 1995.

Langston, C.A.: Structure under Mount Rainier, Washington, inferred from teleseismic body waves. J. Geophys. Res., 84, 4749-4762, https://doi.org/10.1029/JB084iB09p04749, 1979.

Ligorría, J. P., & Ammon, C. J.: Iterative deconvolution and receiver-function estimation. B. Seismol. Soc. Am., 89(5), 1395-1400, https://doi.org/10.1785/BSSA0890051395, 1999.

Longuet-Higgins, M. S.: A theory of the origin of microseisms, Philosophical Transactions of the Royal Society of London. Series A, Mathematical and Physical Sciences, 243(857), 1-35, https://doi.org/10.1098/rsta.1950.0012, 1950.

McFee, B., V. Lostanlen, A. Metsai, M. McVicar, S. Balke, C. Thomé, C. Raffel, F. Zalkow, A. Malek, Dana, et al.: librosa/librosa: 0.8.0, Version 0.8.0, Zenodo, https://doi.org/10.5281/zenodo.3955228, 2020.

Mousavi, S. M., & Langston, C.A.: Automatic noise-removal/signal-removal based on general cross-validation thresholding in synchrosqueezed domain and its application on earthquake data. Geophysics, 82.4, V211-V227. https://doi.org/10.1190/geo2016-0433.1, 2017.

Müller, M.: Fundamentals of music processing: Audio, analysis, algorithms, applications. Cham, Switzerland: Springer International Publishing. https://doi.org/10.1007/978-3-319-21945-5, 2015.

Negi, S. S., Kumar, A., Ningthoujam, L. S., & Pandey, D. K.: An Efficient Approach of Data Adaptive Polarization Filter to Extract Teleseismic Phases from the Ocean-Bottom Seismograms. Seismological Society of America, 92(1), 528-542, https://doi.org/10.1785/0220200034, 2021.

Olofsson, B.: Marine ambient seismic noise in the frequency range 1–10 Hz. The Leading Edge, 29(4), 418-435, https://doi.org/10.1190/1.3378306, 2010.

Pereira, A., Romagosa, M., Corela, C., Silva, M. A., & Matias, L.: Source Levels of 20 Hz Fin Whale Notes Measured as Sound Pressure and Particle Velocity from Ocean-Bottom Seismometers in the North Atlantic. Journal of Marine Science and Engineering, 9(6), 646, https://doi.org/10.3390/jmse9060646, 2021.

Pillet, R., Deschamps, A., Legrand, D., Virieux, J., Béthoux, N., & Yates, B.: Interpretation of broadband ocean-bottom seismometer horizontal data seismic background noise, B. Seismol. Soc. Am., 99(2B), 1333-1342, https://doi.org/10.1785/0120080123, 2009.

Rafii, Z., Liutkus, A., & Pardo, B.: REPET for background/foreground separation in audio. In Blind Source Separation (pp. 395-411). Springer, Berlin, Heidelberg, https://doi.org/10.1007/978-3-642-55016-4_14, 2014.

Rafii, Z., Liutkus, A., Stöter, F. R., Mimilakis, S. I., FitzGerald, D., & Pardo, B.: An overview of lead and accompaniment separation in music, IEEE/ACM Transactions on Audio, Speech, and Language Processing, 26(8), 1307-1335. https://doi.org/10.1109/TASLP.2018.2825440, 2018.

Rafii, Z., & Pardo, B.: Music/Voice Separation Using the Similarity Matrix, Proc. ISMIR, pp. 583-588, 2012.

Ramakrushana Reddy, T., Dewangan, P., Arya, L., Singha, P., & Kamesh Raju, K. A.: Tidal triggering of the harmonic noise in ocean-bottom seismometers. Seismol. Res. Lett., 91(2A), 803-813, https://doi.org/10.1785/0220190080, 2020.

Rondenay, S.: Upper mantle imaging with array recordings of converted and scattered teleseismic waves. Surv. Geophys., 30(4), 377-405, https://doi.org/10.1007/s10712-009-9071-5, 2009.

Romanowicz, B., Stakes, D., Montagner, J. P., Tarits, P., Uhrhammer, R., Begnaud, M., Stutzmann, E., Pasyanos, M., Karczewski, J.F., Etchemendy, S. and Neuhauser, D.: MOISE: A pilot experiment towards

long term sea-floor geophysical observatories, Earth, planets and space, 50(11), 927-937, https://doi.org/10.1186/BF03352188, 1998.

Schlindwein, V., Krüger, F., Schmidt-Aursch, M.: Project KNIPAS: DEPAS ocean-bottom seismometer operations in the Greenland Sea in 2016-2017, Alfred Wegener Institute, Helmholtz Centre for Polar and Marine Research, Bremerhaven, PANGAEA, https://doi.org/10.1594/PANGAEA.896635, 2018.

Schlindwein, V., Wassermann, J., & Scherbaum, F.: Spectral analysis of harmonic tremor signals at Mt. Semeru volcano, Indonesia, Geophys. Res. Lett., 22(13), 1685-1688. https://doi.org/10.1029/95GL01433, 1995.

Skop, R. A., & Griffin, O. M.: On a theory for the vortex-excited oscillations of flexible cylindrical structures. Journal of Sound and Vibration, 41(3), 263-274, https://doi.org/10.1016/S0022-460X(75)80173-8, 1975.

Silver, P.G. & Chan, W.W.: Shear wave splitting and subcontinental mantle deformation. J. Geophys. Res., 96, 16429-16454, https://doi.org/10.1029/91JB00899, 1991.

Snodgrass, F. E., Hasselmann, K. F., Miller, G. R., Munk, W. H., & Powers, W. H.: Propagation of ocean swell across the Pacific, Philosophical Transactions of the Royal Society of London. Series A, Mathematical and Physical Sciences, 259(1103), 431-497, https://doi.org/10.1098/rsta.1966.0022, 1996.

Stähler, S. C., Schmidt-Aursch, M. C., Hein, G., & Mars, R.: A self-noise model for the German DEPAS OBS pool. Seismol. Res. Lett., 89(5), 1838-1845, https://doi.org/10.1785/0220180056, 2018.

Tanimoto, T., Rivera, L.: The ZH ratio method for long-period seismic data: sensitivity kernels and observational techniques. Geophys. J. Int., 172(1), 187-198, https://doi.org/10.1111/j.1365-246X.2007.03609.x, 2008.

Titze, I. R.: Nonlinear source–filter coupling in phonation: Theory, The Journal of the Acoustical Society of America, 123(4), 1902-1915, https://doi.org/10.1121/1.2832337, 2008.

Vaseghi, S. V.: Advanced signal processing and digital noise reduction. Vieweg + Teubner Verlag, https://doi.org/10.1002/9780470740156, 1996.

Wang, R.: A simple orthonormalization method for stable and efficient computation of Green's functions, B. Seismol. Soc. Am., 89(3), 733-741, https://doi.org/10.1785/BSSA0890030733, 1999.

Webb, S. C.: Broadband seismology and noise under the ocean, Rev. Geophys., 36(1), 105-142, https://doi.org/10.1029/97RG02287, 1998.

Webb, S. C., Zhang, X., & Crawford, W.: Infragravity waves in the deep ocean, J. Geophys. Res.-: Oceans, 96(C2), 2723-2736, https://doi.org/10.1029/90JC02212, 1991.

Zahra Zali. (2022). ZahraZali/NoiseCut: NoiseCut (v1.0.0). Zenodo. https://doi.org/10.5281/zenodo.7339552

Zali, Z., Ohrnberger, M., Scherbaum, F., Cotton, F., & Eibl, E. P.: Volcanic Tremor Extraction and Earthquake Detection Using Music Information Retrieval Algorithms, Seismol. Res. Lett., 92(6), 3668-3681, https://doi.org/10.1785/0220210016, 2021.

Zhu, W., Mousavi, S. M., & Beroza, G. C.: Seismic signal denoising and decomposition using deep neural networks. IEEE T. Geosci. Remote., 57(11), 9476-9488. https://doi.org/10.1109/TGRS.2019.2926772, 2019.

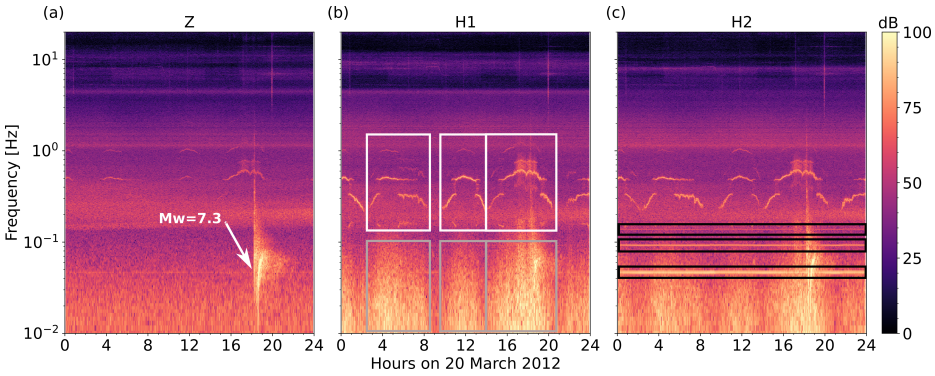

Figure 1: Spectrogram of an one-day OBS signal shows ocean bottom noise on Z (a), H1 (b) and H2 (c) components. The data was recorded by the station D10 of the DOCTAR array with a sampling frequency of 100 Hz. The spectrogram were calculated using a window length of 2^{16} sample and an overlap of 75%. The signal of an earthquake (Mw=7.3) on 20.3.2012 at around 18:00 at the station D10 is shown in (a). The tidal cycle of

the current-induced noise is clearly visible during the high tilt noise episodes (grey box in b). The white box in (b) highlights the tremor episodes caused by the head buoy strumming. On H2 (c) we see an instrument-related, presumably electronic noise (black boxes). The high energy of the secondary microseism band at around 0.2 Hz is visible on all components.

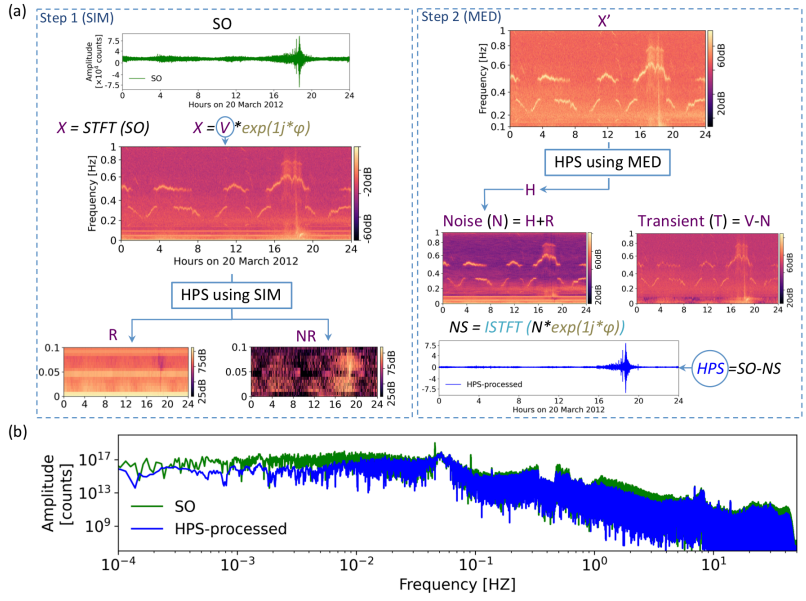

Figure 2: Method flowchart (a) Illustration of the processing steps with a real data example. Left panel shows the first step of the method where using the similarity matrix (SIM) in the frequency range below 0.1 Hz and above 1 Hz, we divide the spectrogram (X) of the original signal (SO) into two spectrograms of repeating (R) and non-repeating (NR) patterns. Right panel shows the second step of the method where we apply a median filter (MED) to the frequency range of 0.1 to 1 Hz (spectrogram X') in order to remove noises from this frequency range. It results in the harmonic spectrogram (H). As the interested frequency range for OBS signals is below 1 Hz, the spectrograms show only this frequency range. Finally the noise spectrogram (N) is created by summing the separated noises derived from two steps and the noise signal (NS) is derived using ISTFT. We obtain the noise reduced signal (HPS) by subtracting the NS from the input OBS signal (SO). STFT, short time Fourier transform. HPS, harmonic-percussive separation. SIM, similarity matrix. MED, median filtering. ISTFT, Inverse Short Time Fourier Transform. (b) Spectrum of the original signal (SO) and the HPS noise reduced signal.

Zahra Zali 28.11.2022 08:48

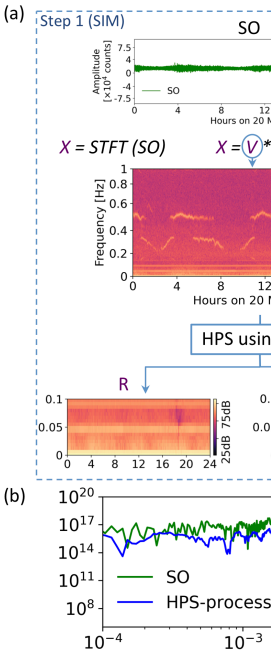

Deleted:

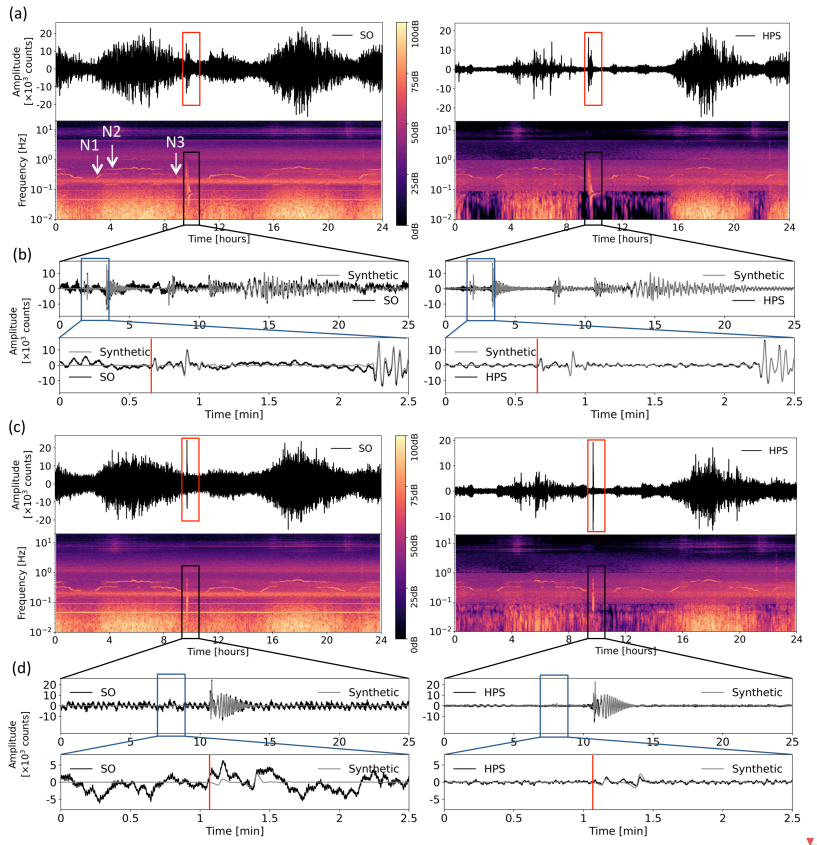

Figure 3: Comparison of the synthetic seismograms and spectrograms of the original signal SO and the HPS noise reduced signal on the R and T components for a synthetic signal with SNR= 1.5 before denoising. (a) & (c) Show one day seismograms and spectrograms for R and T components, respectively. Squares show the earthquake section. The arrows in (a) show three noise situations (N1-N3). (b) & (d) Show seismograms of the earthquake section on SO and HPS signals, with detailed view of the P-arrival (on component R in subfigure b) and SH-arrival (on component T in subfigure d). Red lines show P-arrivals in (b) and SH-arrival in (d).

Zahra Zali 28.11.2022 08:47

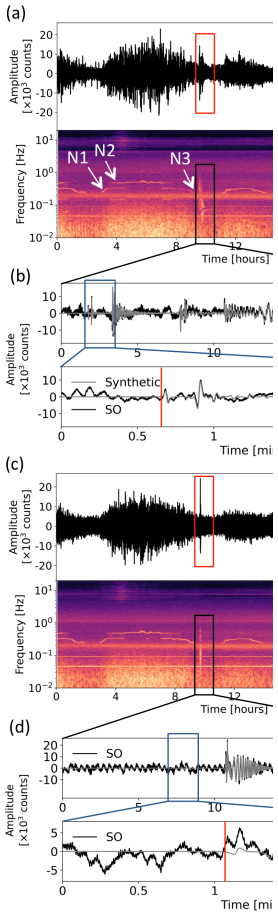

Deleted:

Zahra Zali 24.11.2022 12:53

Deleted: (SNR is defined as RMS of the signal divided by RMS of the noise)

Zahra Zali 24.11.2022 12:55

Deleted: The spectrograms clearly show the reduced noise level on the HPS signal.

Zahra Zali 24.11.2022 12:56

Deleted: The whole amplitude and the phase information of the synthetic earthquake are preserved in the HPS signal but it's very less noisy compared with SO.

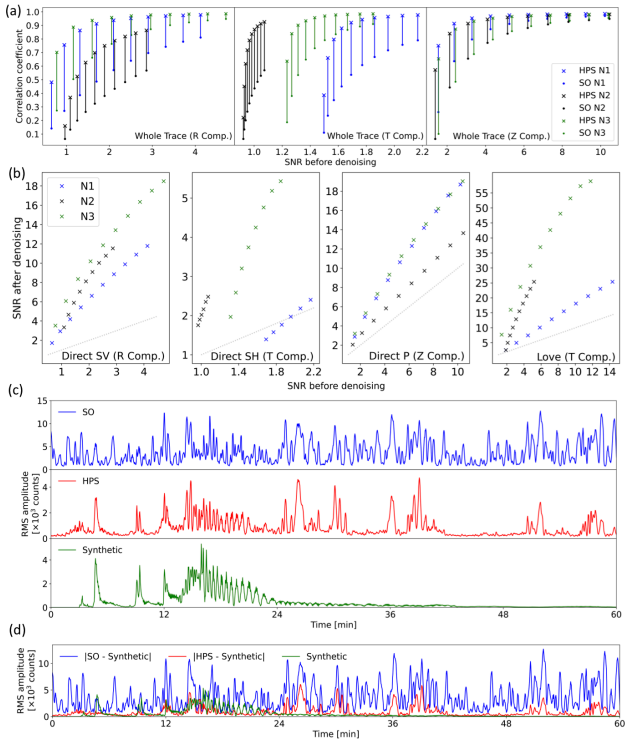

Figure 4: Comparison of the synthetic SO and HPS signals (both are lowpass filtered at 1Hz). (a) Correlation coefficients (for the whole trace) for different SNRs and 3 realistic noise realizations for Z, R and T components (Component is abbreviated as Comp.). (b) Improvement of SNR for direct body wave phases and the Love wave. The gray dotted lines in (b) mark the line with gradient 1 (no improvement of SNR). (c) Comparison of the root mean square (RMS) amplitude of one example of the SO, HPS and synthetic earthquake signals. This signal is the same example shown in Fig. 3 (R component, SNR= 1.5 before denoising). (d) The RMS of the original noise (blue trace: |SO - Synthetic|) and the remained noise after denoising (red trace: |HPS- Synthetic|) compared to the synthetic earthquake signal.

Zahra Zali 24.11.2022 13:07

Deleted: We see significant improvement in both correlation coefficient and SNR for all the realizations after denoising.

Zahra Zali 24.11.2022 13:09

Deleted: The HPS signal has significantly lower energy compared with SO due to noise reduction, but has almost similar energy compared with the synthetic earthquake which shows the energy of the earthquakes and all the phase arrivals are well preserved during the denoising process.

Zahra Zali 24.11.2022 13:09

Deleted: A high noise reduction is seen in the red trace compared with the blue one and the remained noise has an inconsistent pattern compared to the synthetic earthquake that confirms denoising process doesn't modify the earthquake energy and its phase arrivals.

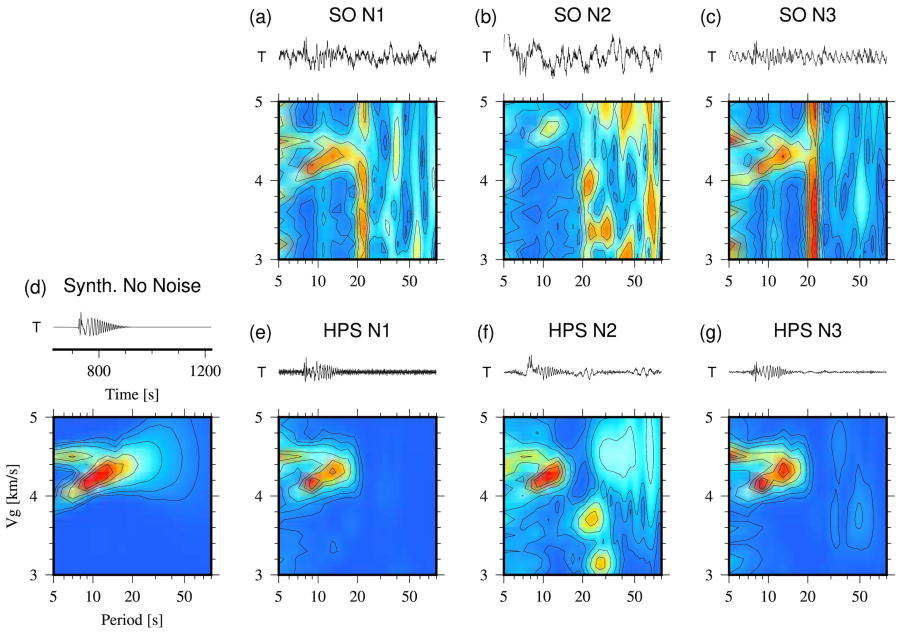

Figure 5: Love wave group velocity analysis for unfiltered and HPS processed synthetic Love wavetrains contaminated by three real world OBS noise signals (noise situations N1-N3, station D10, DOCTAR experiment, see Sect. 2 for more details). (a)–(c): Lower panels: Unfiltered synthetic signal (SO) MFT analysis results. Top panels: seismogram time windows corresponding to the range of group velocities shown on the y-axis. (d) Noise free synthetic case. (e)–(g): HPS processed input traces for noise situations N1-N3 (lower panel: MFT analysis result, top panel: HPS processed seismogram).

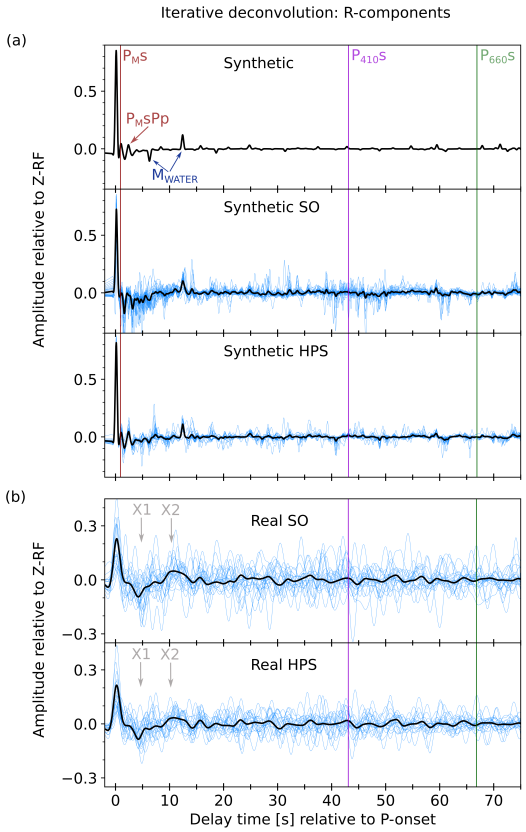

Figure 6: R-receiver function comparison of synthetic and real data examples. (a) Comparison of the synthetic data examples, lowpass filtered at 2 Hz. The pure synthetic R-RF is shown in the uppermost panel, followed by the synthetic SO and the synthetic HPS R-RFs. The black lines show the summed individual R-RFs (blue waveforms). The theoretical onset times for this specific model are marked. Red line: Ps-arrival of the Moho (P_MS) and its multiple (P_MSPp), violet line: Ps arrival of the 410 ($P_{410}S$), green line: Ps-arrival of the 660 ($P_{660}S$), dark-blue arrows: Multiples in the watercolumn of 4.9 km (M_{WATER}), repetitive every 6.5s. (b) Comparison of the real data, bandpass filtered at 0.05–0.5 Hz. The upper panel shows the R-RFs of the real SO traces and the lowermost panel the R-RFS of the real HPS traces. The individual traces (blue) are shown as stack (black line) and the theoretical onset times based on the average ak135 velocity model are shown as violet line ($P_{410}S$) and green line ($P_{660}S$). The origin of the phases X1 and X2 (grey) remain unclarified, since their interpretation is beyond the scope of this study.

Table 1: Parameters values used in our study

Parameters	Frequency range for SIM	Frequency range for MED	FFT window size	FFT overlapping percentage	Waiting factor in SIM	Kernel size in MED
Values	[0-0.1] & above 1 Hz	[0.1-1] Hz	16384 samples	75%	2 hours	80